Aerospace Science and Technology xxx (xxxx) 109745

Contents lists available at ScienceDirect

Aerospace Science and Technology

journal homepage: www.elsevier.com

Journal logo

Tension-twist coupling morphing wing using a novel mechanical metamaterial

Xueren Zhu [a, b], Jiaying Zhang [b, *], Wei Chen [a, **], Huaiyuan Gu [c]

[a] Power Beam Processiong Laboratory, AVIC Manufacturing Technology Institute, Beijing 100024, China
[b] School of Aeronautical Science and Engineering, Beihang University, Beijing 100190, China
[c] Department of Aerospace Engineering, Queen's Building, Bristol, BS8 1TR, UK

ARTICLE INFO

Jang-Kyo KIM

Keywords:
Morphing wing
Tension-twist coupling
Metamaterial
Cell stacking
Structural design

ABSTRACT

A novel tension-twist coupling morphing wing is proposed using tension-twist coupling metamaterials as the wing spar. The tension-twist coupling deformation was achieved by stacking of unit cells with tension-shear coupling behaviour. A finite element model was created to study the coupling behaviour of the unit cell, where the effect of cell configuration on the tension-shear coupling properties were numerically explored. The tension-twist coupling of the metamaterials was analysed and validated by a set of static tests using samples fabricated by selective laser sintering (SLS). The metamaterial was then implemented into a morphing wing to achieve adaptive twist. It was found that a valuable wing twist can be achieved by a relatively small actuation force, which can lead to a significant improvement in the overall aerodynamic performance. This novel way of realising the twist deformation of morphing wing reduces the demand for its driving system.

1. Introduction

The morphing aircraft can adjust its aerodynamic shape continually to adapt to various flight conditions and missions[1–4]. Their advantages over conventional aircraft regarding safety, adaptability, efficiency and controllability have aroused increasing attention and substantial research interest[5,6]. By changing the shape, the morphing aircraft can perform optimally in different flight conditions[7–10]. Integrating smart materials, flexible skin and deformable structure shows promising potential for achieving morphing aircraft's flexible, continuous and smooth deformation. In 1973, an experimental work conducted by Boeing showed that a continuous and seamless change of wing shape could significantly increase the aerodynamic efficiency [11]. Lockheed Martin developed a Z-folding morphing aircraft capable of a 440% change in the wing aspect ratio and a 145% change in the wing area, leading to an improved performance during different flight missions such as surveillance, cruise and rapid manoeuvring [12].

The active twisting wing can enhance aerodynamic performance, such as lift and drag characteristics, through adjusting the angle of attack of its ribs [13,14]. Research published by Majji in 2007 presented a twistable morphing wing, which enhanced the operating envelope of the wing's angle of attack[15]. The wing was rigidly coupled to four telescoping tubes independently attached to the wing along the span, which benefits the twisting of the wing. A set of meshing gears was installed on the shaft and the beam to achieve the twisting of the wing when driven by a motor inside the wing root[16]. A wing morphing skeleton mechanism was proposed for the morphing wing, enabling the wings to change their shapes by bending, twisting and sweeping, and an enhanced aerodynamic performance was achieved[17]. Introducing smart materials such as shape memory alloys has also diversified the twisting wings design[18]. An experimental wing was demonstrated, which was able to twist approximately 10° using an inductively heated SMA torsional actuator[19]. Furthermore, structures with special deformation effects have also been widely studied for designing the twisting wings. Tensegrity structure was demonstrated to show attractive potential for twist deformation. The approach to implementing the tensegrity structure onto the twisting wing was discussed, and the spanwise twist was achieved[20,21].

Mechanical metamaterials, whose unique properties are achieved by artificial tailoring of the unit cells, have a potential capability to designing the twisting wing. In addition to properties such as negative Poisson's ratio[22,23], ultralight and ultra-stiff lightweight[24,25], metamaterials can achieve special deformation characteristics which is impossible to achieve through ordinary materials[26,27]. A digital

* Corresponding author.
** Corresponding author.
E-mail addresses: jiaying.zhang@buaa.edu.cn (J. Zhang), chenw084@avic.com (W. Chen).

https://doi.org/10.1016/j.ast.2024.109745
Received 8 July 2024; Received in revised form 14 October 2024; Accepted 13 November 2024

twisting wing constructed from discrete lattice unit cells was reversibly assembled and tested in the subsonic wind tunnel, which demonstrated stall mitigation by wing twist[28,29]. Diamond-shaped cells were joined to enable a planar twist of the morphing wing in clockwise and counterclockwise directions[30]. An optimal actuator placement and position optimization were also explored. Metamaterials with tension-twist coupling (TTC) characteristics are particularly of interest since they have shown great potential to be used in flexible wings and alter the lift distribution by passively or semi-passively adjusting the angle of attack (AoA)[31]. Mechanical metamaterials that exhibit the designable ability to twist deformation, which achieve the required spanwise twist deformation have been extensively studied[32–37]. Frenzel [38] realized a twist by designing microstructured three-dimensional elastic chiral mechanical metamaterials, which increase degree of freedom of the system. 3D compression-torsion metamaterials were proposed based on a chiral mechanism[39,40] and were refined with thermal-torsion properties to achieve a more noticeable twist under both temperature change and uniaxial load[41].

A large number of tension-twist coupling metamaterials had been developed, such as chiral mechanical metamaterials[38]. However, most of the tension-twist coupling metamaterials remain in the design stage, and few of them have been applied to the design of morphing wings[28]. This paper illustrates a twist morphing wing that based on a proposed novel metamaterial with bend-twist coupling property [42,43], where the unit cell is shown in Fig. 1(a). The unit cell, a type of 3D lattice meta-material, comprises a simple cube and a frame formed by overlapping two cross grids along the diagonal plane. The relative density can be calculated as follows:

$$\bar{\rho} = \frac{2a + b + h + 2\sqrt{b^2 + h^2} + 2\sqrt{a^2 + b^2 + h^2}}{abh}\pi(d/2)^2 \tag{1}$$

In addition to the reported properties, it has been found that the unit cell showed excellent tension-shear coupling properties. This is due to the change in the cell symmetry condition by introducing a sub-cell to reinforce the diagonal plane. Consequently, shear strain is induced by applying a uniform tensile loading. A tailored strategy for cell stacking, as shown in Fig. 1(b), involves arranging the unit cells in different location to achieve shear in the targeted orientations so that the tension-twist coupling property can be generated in the macrostructure. In other words, where a uniaxial load apply on the macrostructure, a torque can also be obtained by the induced shear strain of the cells, as depicted in Fig. 1(c). Subsequently, the metamaterial designed with a targeted tension-twist coupling (TTC) property is then implemented into a morphing wing to achieve active twist, as shown in Fig. 2. Finally, the preliminary design of the wing is further investigated using Computational Fluid Dynamics (ANSYS FLUENT 2023R2) to assess the aerodynamic performances[44].

This paper is organised as follows. Section 2 presents the design method of tension-twist coupling metamaterials, where the elastic modulus and coupling deformation properties of the unit cell are characterised. Next, the tension-twist coupling deformation of the metamaterials is achieved using a proposed design process. Then, section 3 illustrates a set of static experiments, which is conducted to validate the tension-twist coupling properties of metamaterial designed in various configurations. In Section 4, a novel morphing wing is designed where the metamaterial is employed as the wing spar to achieve wing twist. The aerodynamic characteristics of the morphing wing are further discussed, and the designed twisting wing as the morphing part. The advantages of the morphing wing on the lift coefficient and the lift-drag ratio are demonstrated through CFD simulation. However, few studies exist have explored the employment of mechanical metamaterials for achieving twist deformation in morphing wing. The introduction of metamaterials enables a valuable wing twist achieved by a relatively small actuation force, while maintaining a low weight. The implementation of twisting morphing wing can remove the design limits of morphing wing imposed by traditional driving system.

2. Tension-twist coupling metamaterials

2.1. Tension-shear coupling metamaterials

The 3D lattice metamaterials can be classified into bending-dominated and stretching-dominated[45]. It depends on the deformation behaviours of the struts in the unit cells under loading. The deformation behaviours of unit cells indicate its different failure mechanisms. The Maxwell criteria[45] can be applied to determine the type of unit cell as

$$M = s - 3n + 6 \tag{2}$$

where s and n represent the number of struts and nodes in a unit cell, respectively. It can be calculated that M is equal to -7, for $s = 26$ and $n = 13$, suggesting the unit cell is bending-dominated. The struts' deformation mechanism, bending while stretching, determines the element type, which is the basis for numerical simulation. Then, finite element analysis (FEA) is employed to analyse the metamaterials' elastic modulus and tension-shear coupling properties.

The elastic modulus of the metastructure stacked by the unit cells was first analysed by FEA. When assembled into a 3D lattice metamaterial, it demonstrates a tunable elastic modulus performance and high specific stiffness, maintaining considerable stiffness at a low relative density. A set of cubic models was created in ABAQUS 2022, stacked by

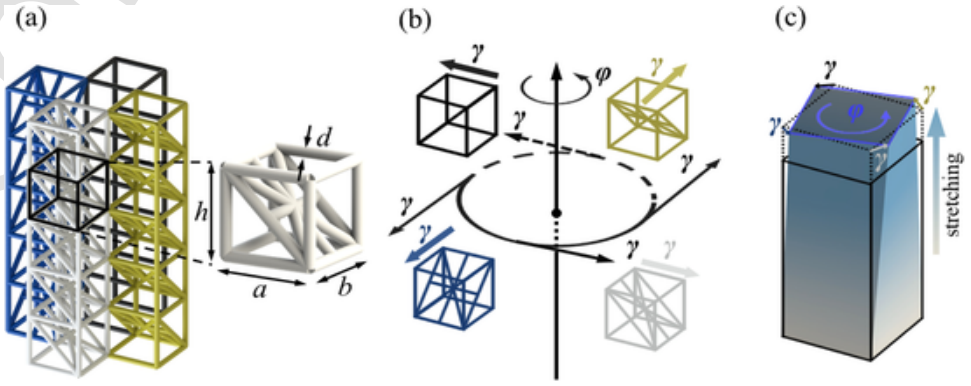

Fig. 1. (a) The unit cell of the three-dimensional lattice metamaterial; (b) Assembly of unit cells to generate the twist around axis; (c) Generation of twist induced by shear strains when the metamaterial is stretching.

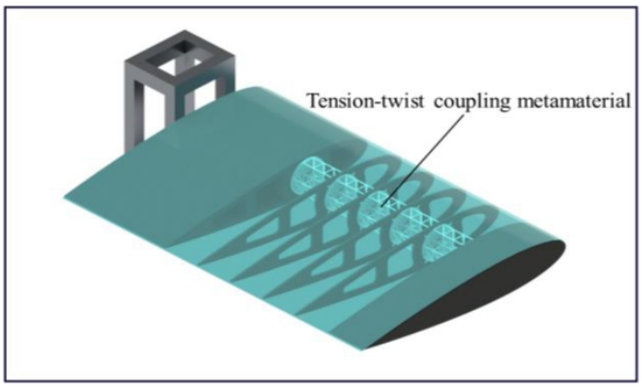

Fig. 2. Concept for the morphing wing using a tension-twist coupling metamaterial as the wing spar.

unit cells that are also cubic, as shown in Fig. 3(a). The L and a represent the size dimensions of cubic structures and unit cells, respectively. The normalized width of the cubic model, L / a, ranges from 1 to 15, while $a = 5$ mm. The struts have a circular cross section with a diameter d and several different diameters ($d = 0.25$ mm,0.5 mm,0.75 mm and 1 mm) were designed to investigate the relation between diameter and elastic modulus. Additionally, the struts in unit cells were meshed using ten Timoshenko beam elements (element code 'B31' in ABAQUS) to guarantee mesh independence. *OXYZ* represents the coordinates of the global geometry, while *oxyz* represents the local coordinates of the unit cell. Nylon (PA12) was used here with a modulus, E_S, of 800 MPa and Poisson's ratio, ν, of 0.35, which is listed in Table 1. A uniform stress, σ_{app}, was applied on the top face while the bottom face was constrained. The modulus can be calculated by dividing the uniaxial strain by the applied stress as

$$E^* = \frac{\sigma_{app}}{\varepsilon_{zz}} \tag{3}$$

where E^* represents the equivalent elastic modulus of the macro-structure, ε_{zz} represents the axial strain along the *Z*-axis and σ_{app} represents the applied stress.

Additionally, the influence of the number of meshed elements per strut on the analysis results is demonstrated in Fig 3(b), using the cubic structure with a normalized width of $L / a = 10$ as an example. The convergence of the finite element analysis is verified as the results of FEA approach a mesh-independent value when the number of elements per strut reaches 10.

The FEA results are presented in Fig. 4, where the elastic modulus of the metamaterial, E^*, is normalized by the modulus of the constituent material, E_S. It can be observed that the normalized modulus, E^*/E_S, reduces asymptotically with an increase in the aspect ratio L / a and reaches a size-independent value when L / a is greater than 12. The size-independent normalized elastic modulus of the metamaterial is approximately proportional to the square of the diameter, d^2, of its struts. Through calculation, the metamaterials maintain a similar specific stiffness, $E^*/E_S/\overline{\rho}$ of 0.113, regardless of the diameter of the struts.

A FEA model was created using ABAQUS 2022 to study the coupling behaviour of the metamaterial, as shown in Fig. 5. Each cell strut was meshed by ten Timoshenko beam elements (element type B31 in ABAQUS) with the material properties listed in Table 1. Fig. 5(b) illustrates that a shear strain was induced due to its asymmetric nature when a uniform tensile load is applied. A set of unit models with different dimensions (h/b and a/b) was created to study the influence of the characteristic dimensions. The cell width, b, and diameter, d, were 8 mm and 0.5 mm, respectively. The characteristic size, h/b, ranged from 1 to 5 and a/b was selected as 1/4, 1/3, 1/2, 1, 2, 3 and 4. An axial tensile force, F_Z, was applied on the top nodes of each model while the bottom nodes were fully fixed. The ratio between activated shear strain, ε_{zx}, and axial strain, ε_{zz}, was calculated to assess the coupling properties of unit cells.

Fig. 6 shows different unit cells can provide varying tension-shear coupling properties under uniaxial loading due to their asymmetric cell geometries. It can be seen that cells with the same characteristic size (a/b) show coupling properties directly proportional to the ratio (h/b). Furthermore, cells with a higher (a/b) ratio exhibit higher coupling properties. It can be seen that the slopes of the curves are equal to (a/b) value of the corresponding cells.

2.2. Tailored tension-twist coupling metamaterial

Tension-twist coupling (TTC) deformation can be achieved by stacking the unit cells described in Section 2.1. Firstly, a cell library is established based on the coupling properties of the unit cells, as shown in Fig. 7(a). The serial number of each unit cell represents it has different coupling characteristics. In this paper, four types of unit cells, numbered from 1 to 4, with different orientations of shear strains are selected to fill the cell library for potential tension-twist coupling. Each adjacent cell is connected through sharing nodes and faces so that effective stacking can be achieved, as shown in Fig. 7(b). Then, the unit cells are stacked with grade from 1D to 3D to create metamaterials with tension-twist coupling properties, as shown in Fig. 7(c). The tension-twist coupling metamaterials are created by assembling the tension-shear coupling cells in four different orientations, as shown in Fig. 1(b,c). Therefore, when a uniform tensile load applied to the material, a twist

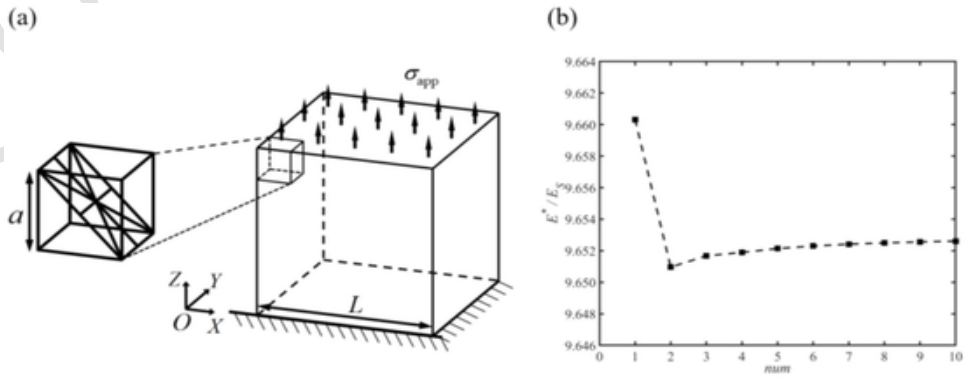

Fig. 3. Modeling and mesh independence analysis of the FEA. (a) Modeling of the cubic macro-structure; (b) Convergence verification of FEA.

Table 1
Material properties used in the model.

a (b,h)/mm	Material	E_S/MPa	ν	Tensile stiffness/MPa	Breaking Elongation/%
5	Nylon (PA12)	800	0.35	33.3–39.8	11–19

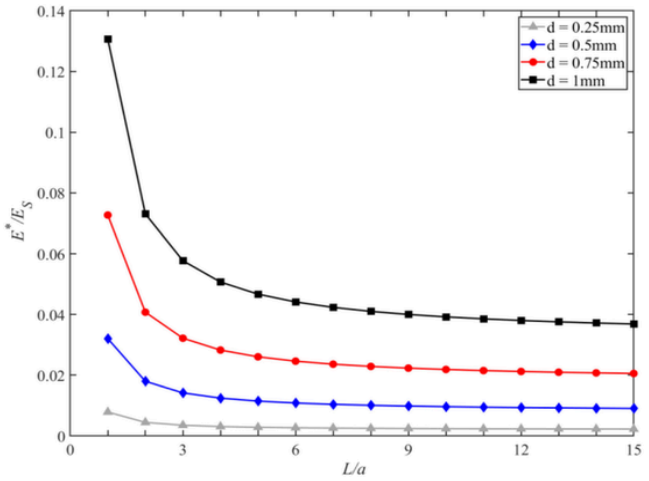

Fig. 4. Normalized modulus of the metamaterial with different numbers of unit cells.

is induced due to the coupled shear strain in each unit cell. It transforms the coupled tension-shear deformation of unit cells into the coupled tension-twist deformation of the metamaterials. Stacking metamaterials allows for the accumulation and superposition of twist deformation layer by layer.

The purpose of the proposed tension-twist coupling (TTC) metamaterial are designed for morphing wing, so that a cantilever beam is studied here as the wing spar. Three types of cantilevers with TTC properties were created with the proposed design process, as illustrated in Fig. 8. In each type, the unit cells within the cantilever section are arranged in a rotationally symmetrical distribution around the central axis, consistent with the stacking strategy described in Fig. 1(b). Upon stacking, the coupled tension-shear deformation of the cells is converted into the coupled tension-twist deformation of the cantilevers. When the cantilevers are extended through arraying, the twist deformation of adjacent sections accumulates and superimposes due to stacking. A remarkable macroscopic tension-twist coupling (TTC) deformation can be observed in the cantilevers. As shown in Fig. 8(b), these three cantilevers with a same section area are named as two-cells combined cantilever, four-cells combined cantilever and cross-shaped cantilever, respectively. The twisting direction in each cantilever is intentionally designed to be consistently clockwise for comparison. Previous research has indicated that the characteristic sizes of the unit cell are governing parameters determining the tension-shear coupling effect. Therefore, the tension-torsion coupling effect can be adjusted by modifying the constituent unit cells' characteristic sizes, h/b and a/b.

The FEA was carried out using ABAQUS 2022 to analyse the deformation of the proposed cantilevers under a specified tension. The 'B31' elements were employed to mesh the FEA models for the trusts within the cantilevers, and each truss was meshed into ten elements to ensure convergence. The cantilever models were fully fixed at one end while the other end was suspended and subjected to uniaxial tension. The length of the cantilever beam is 200 mm, and the diameter of the struts in the unit cells is 2.3 mm. The inner cells of the two-cells combined cantilever are rectangles with sizes of $a = 40$ mm and $b = h = 20$ mm, respectively. The four-cells combined cantilever and the cross-shaped combined cantilever has the same cube-shaped inner cells with sides of $a = b = h = 20$ mm.

Fig. 9 shows the deformation along the z-axis in the three cantilevers. A pair of opposite strains can be observed on two sides of the cantilever section, which are linearly distributed along the central axis. This indicates that the cantilevers exhibit twist deformation under uniaxial tension. The finite element analysis (FEA) results confirmed the feasibility of the tension-twist coupling meta-structures. Fig. 10 compares the twist deformation of these three cantilevers under an axis strain, ε_X, of 0.01. The twist of cantilevers generated by different stacking modes is quite different under the same axis strain. Specifically, the cross-shaped combined cantilever exhibits the most significant twist angle, followed by the four-cells combined cantilever, which exhibits a similar twist angle. The two-cells combined cantilever exhibits the smallest twist angle which is approximately half of the other two cantilevers. Notably, the twist angle increased linearly from the hub to the tip under a uniaxial tensile load, and it is attributed to the effect of stacking, which enables the accumulation and superposition of twist deformation across the adjacent layers.

2.3. 3. Experiment validation

In this section, the coupling properties of the tension-twist metamaterials are experimentally investigated in a cantilever beam configuration, as shown in Fig. 11. First, the proposed tension-twist metamaterials are fabricated by Selective Laser Sintering (SLS) with Nylon (PA12). The samples were then loaded by hanging weights on the free end, whereas the other end was fully fixed by an industrial bench vice. The induced twist angle, φ, was measured using laser sensors to capture the

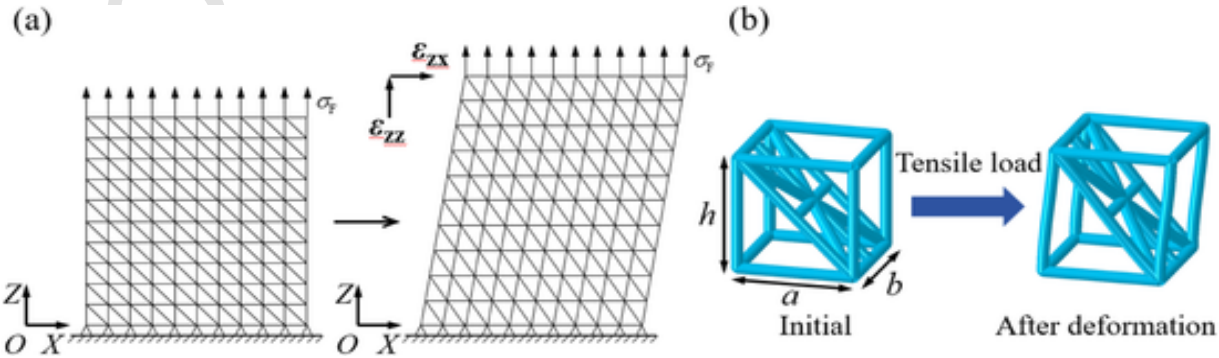

Fig. 5. Tension-shear coupling mechanism. (a)Tension-shear coupling deformation of metamaterial under uniaxial tensile load; (b) Fundamental coupled deformation mode.

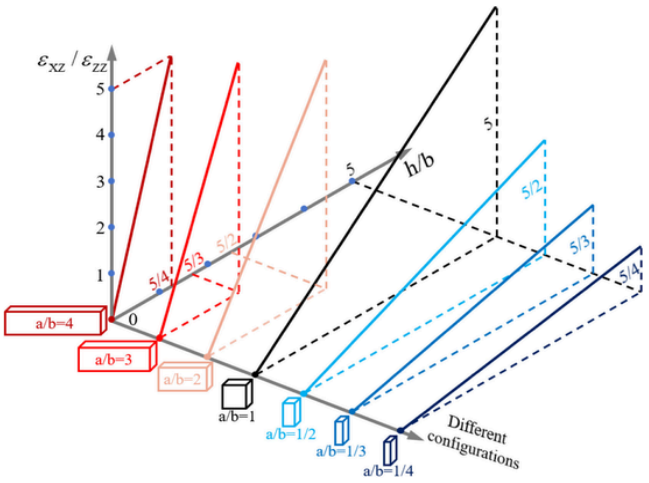

Fig. 6. Coupling properties of various unit cells with different characteristic sizes.

coupling effects. The Digital Image Correlation (DIC) method is also employed for measuring the full-field displacement of samples subjected to the applied loads, as shown in Fig. 11(b).

The three types of cantilevers, which are proposed in Fig. 8(b), are composed of four parts i.e. root clamping section, loading pin, lattice section and tip bar to allow for the twist measurement, as shown in Fig. 11(a). The fabricated struts in the samples have an average diameter of 2.3 mm with an error of 0.1 mm, measured by vernier scale. Additionally, several samples of the two-cells combined cantilever with different lengths of metamaterial section (the lattice section's lengths of 200 mm, 160 mm, 120 mm and 80 mm, respectively) were fabricated to investigate the influence of the stacking layers' number on twist angle. To prevent the distortion of boundary due to torque during the stretching process and enable the application of tension force, a top block named 'loading pin' was added at the forced end of the experimental cantilevers. The twist angle was measured using laser sensors (Panasonic HG-C1100 with the measurement range of 65–135 mm and the accuracy of 70 μm), which light on the tip bar, as shown in Fig. 12. The twist angle is calculated as

$$\varphi = \tan^{-1}\left(\frac{\mathbf{d_{AB}}}{\mathbf{d_{OA}}}\right) \tag{4}$$

where d_{AB} represents the distance of the tip bar swept along the direction of laser beam and d_{OA} represents the distance between the center of terminal surface and the spot where the laser light on. As increasing uniaxial loads were applied to the loading pin, a progressively significant twist angle can be observed on the cantilevers.

The TTC properties of metamaterials are investigated experimentally and subsequently compared with the results obtained from finite element analysis (FEA). The twist deformation of these cantilevers was analyzed through ABAQUS 2022 with the same models used in *Section 2.2* and a variable axial force was applied to each model. The stacking methodology and longitudinal superposition mainly affect the TTC properties of the metamaterials. The stacking methodology involves the stacked unit cells' selection and the assembly modes. Longitudinal superposition refers to the number of stacked layers and the twist deformation generated in each cross section can be superposed layer by layer. The results of FEA and DIC for the designed cross-shaped combined cantilever are illustrated in Fig. 13, while the applied axial tensile force gradually increases up to 50 N. The results obtained from the DIC and FEA exhibit a significant agreement. Twist of the sections along *y*-axis can be found increasing gradually from the root clamping section to the loading pin. The twist angle at the loading pin becomes increasingly significant with increased applied tensile load, suggesting more effective coupling is achieved.

Fig. 14 demonstrates the relationship between the twist angle of the meta-structures and the applied uniaxial tensile force. During the stretching process, all three types of cantilevers exhibit a similar deformation mechanism—twist occurs under the tensile load and is directly proportional to the applied tensile force. Among the cantilevers, the four-cells combined cantilever exhibits the largest twist deformation, followed by the cross-shaped combined cantilever, while the two-cells combined cantilever exhibits the smallest twist angle, under the same uniaxial tensile force. It indicates the most effective coupling achieved in the four-cells combined cantilever, followed by the cross-shaped and two-cells combined cantilever. When a tensile force of 50 N is applied, the twist angles are measured as 0.706°, 0.614° and 0.504°, respectively. The results obtained from FEA and experiment for the meta-structures are significantly agreed. The coupling coefficient, k_C, is defined as the gradient of the lines representing the FEA results in Fig. 14(a). k_{C1}, k_{C2} and k_{C3} represent the cou-

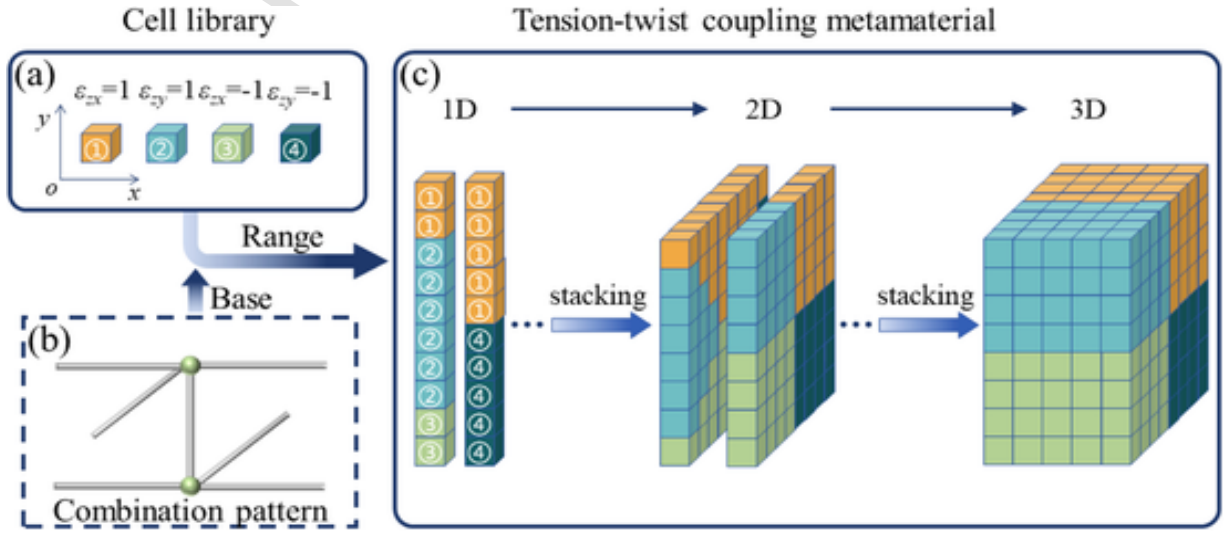

Fig. 7. Design process of tension-twist coupling metamaterials.

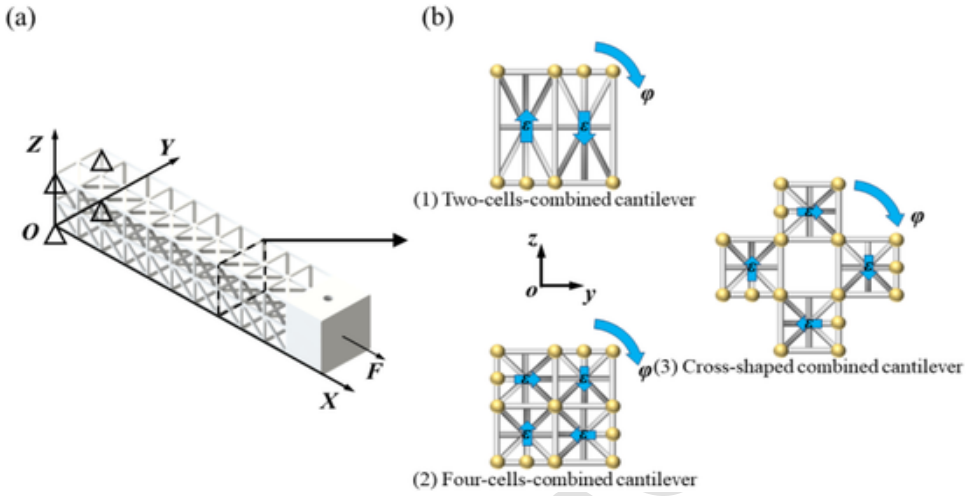

Fig. 8. Cantilevers with tension-twist coupling property: (a) Schematic of cantilever beams produced by stacking of cells; (b) Three types of cantilever with coupling effect.

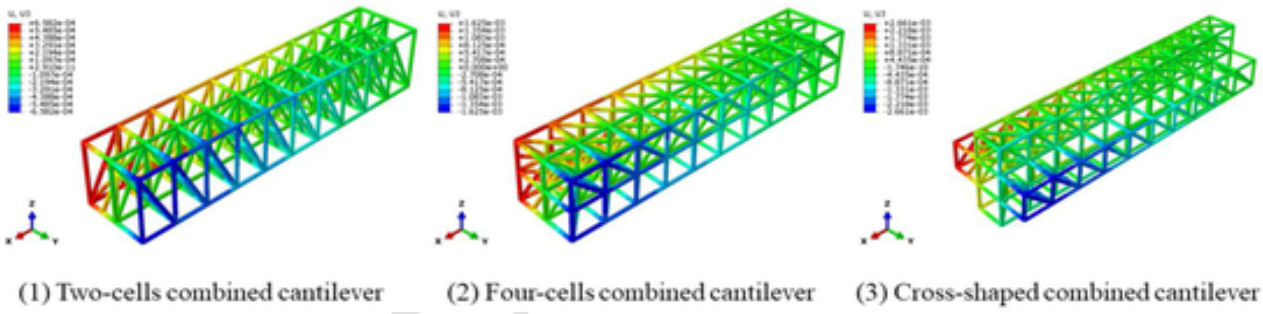

Fig. 9. Results obtained from FEA when $\varepsilon_X = 0.01$.

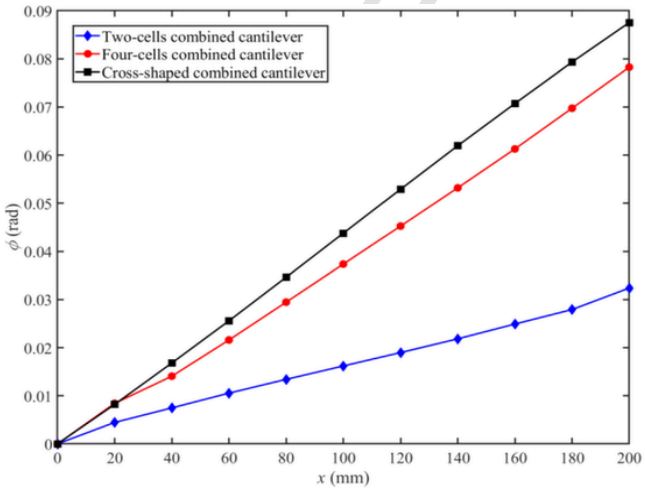

Fig. 10. Distribution of the twist angle for cantilevers with different stacking strategies when $\varepsilon_X = 0.01$.

pling coefficient of the cross-shaped combined cantilever, the four-cells-combined cantilever and the two-cells-combined cantilever, respectively. Notably, it can be calculated that $k_{C2} > k_{C1} > k_{C3}$. Interestingly, contrary to the results in Fig. 14(a), a higher coupling effect was achieved by the cross-shaped combined cantilever ($k_{C1} > k_{C2}$), as shown in Fig. 10. The reason is that more axial rods held within the cross-shaped combined cantilever, results in enhanced axial stiffness, and lower shear strains can be utilized to assemble the twist deformation under a specific axial force. In other words, the cross-shaped cantilever exhibits a more effective coupling under the same axial strain (Fig. 10), but smaller twist angle under an equivalent axial tensile load compared to the four-cells combined cantilever (Fig. 14(a)). The coupling coefficients and weights of the cantilevers are listed in Fig. 14(b) to compare the specific coupling effect of the cantilevers. The coupling coefficient of cantilevers are 2.2258, 2.5409 and 1.8683, with corresponding masses of 321.93 g, 319.94 g and 311.31 g, respectively. The difference in mass among the cantilevers is attributed to the difference in the number of layers stacked within the metamaterials. By dividing the coupling coefficient by the corresponding mass, it can be calculated that the four-cell combined cantilever has the highest specific coupling effect, followed by the cross-shaped combined cantilever, while the two-cell combined cantilever has the lowest specific coupling effect.

When the twist orientation of each layer is consistent, the twist deformation generated in each layer can be accumulated and superposed under stacking. FEA was conducted to study twist performance within the meta-structure, using the designed two-cell combined cantilever as an example. A change in length (referring to the number of layers stacked in a cantilever) and a constant force of 50 N were applied for analysis. Cantilevers of the corresponding lengths were prepared and tested, with the results in Fig. 15. It is observed that the twist angle of

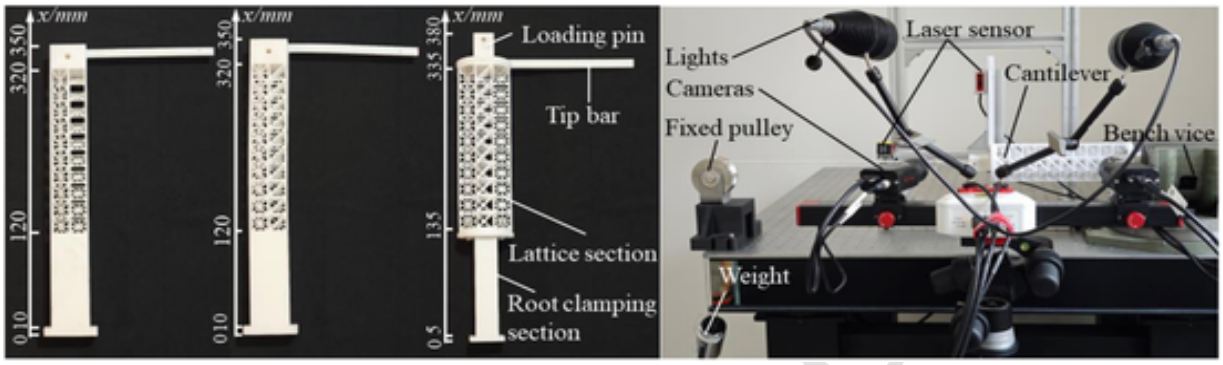

Fig. 11. Samples and experiment: (a) Samples of the cantilevers fabricated by SLS; (b) Experimental equipment(including the tension application equipment and DIC equipment).

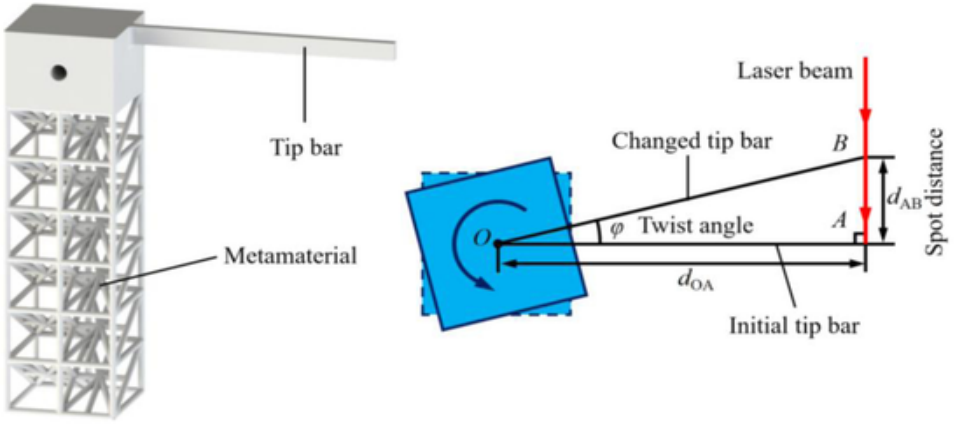

Fig. 12. Schematic of twist angle measurement for the cantilever samples.

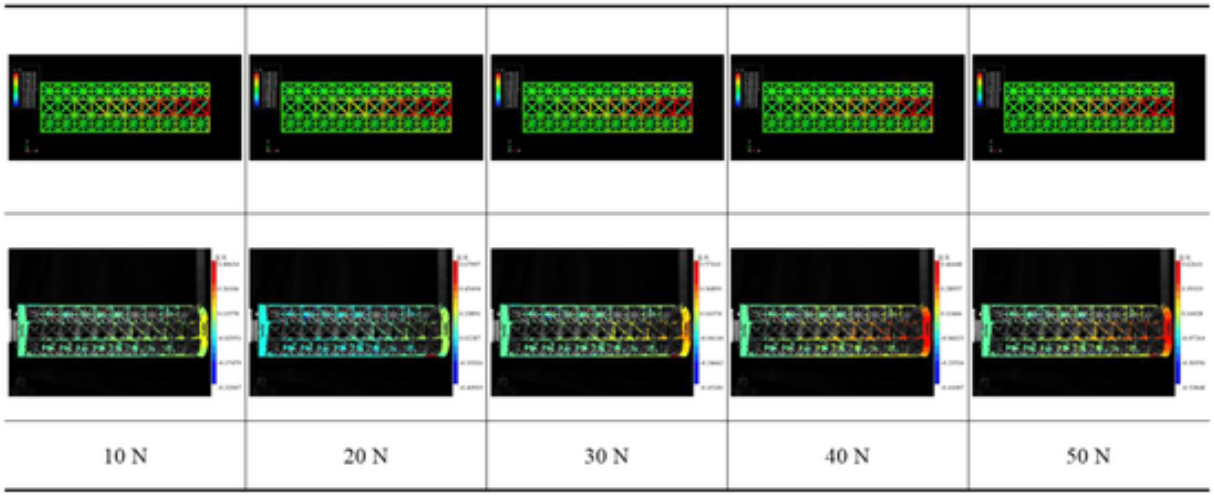

Fig. 13. The results obtained from FEA and DIC.

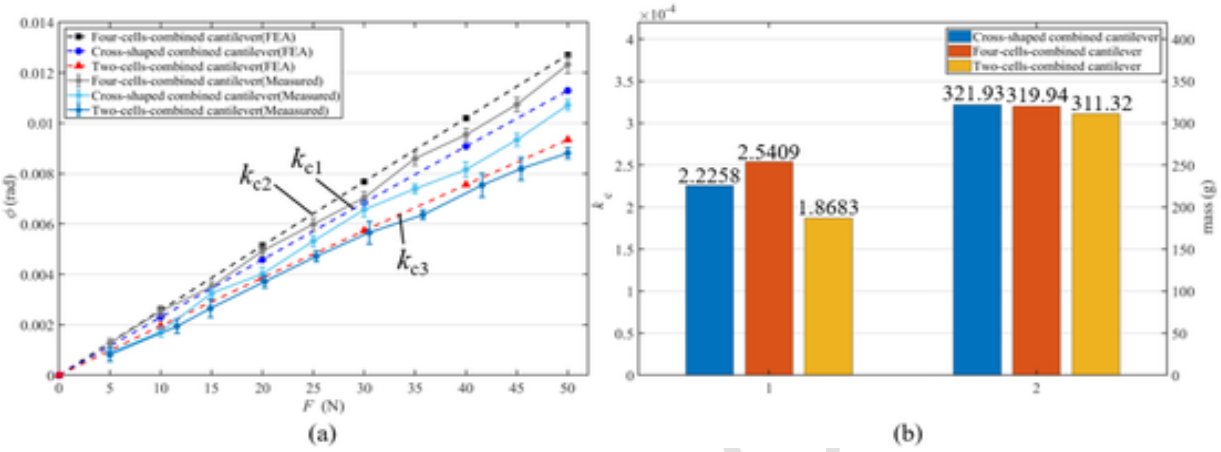

Fig. 14. (a) Relation between twist angle and tensile force for the cantilevers; (b) Comparison of twisting coupling coefficient and masses of cantilevers.

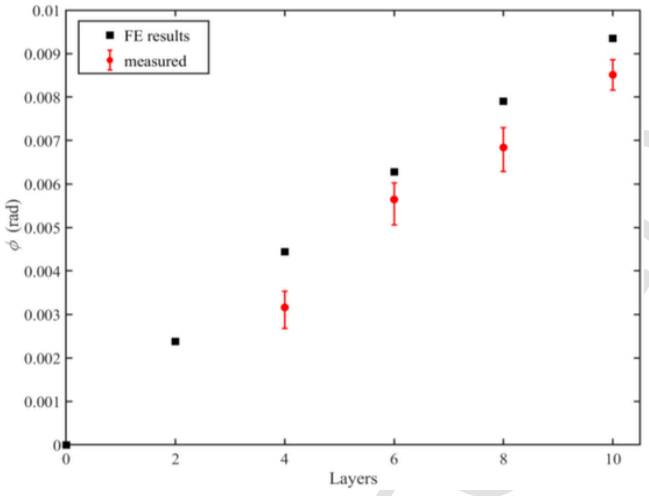

Fig. 15. Relation between twist angle of the cantilevers and the number of stacking layers.

the meta-structures increases linearly with the number of layers stacked along the longitudinal direction. The results obtained from testing and FEA demonstrate a significant arrangement.

4. Morphing wing using tension-twist coupling metamaterial

4.1. Twist morphing

The metamaterials with tunable TTC properties are used to design a wing spar to achieve adjustable and continuous twist deformation, as illustrated in Fig. 16(a). Tension is applied to the metamaterial through a linear motor positioned within the root of the twisting wing. Wing ribs are connected to the wing spar via mortise-and-tenon joints and distributed evenly along the wing spar. When subjected to axial tension, the wing twists due to the TTC effect of the metamaterial. The twist angle between adjacent wing ribs is equal due to the linear distribution of the twist angle in the meta-structure. Introducing a tension-twist coupling metamaterial as the wing spar can simplify the drive mechanism and improve control effectiveness enabling the multi-dimensional deformation of wings with input from a single direction.

A physical prototype of the designed twisting wing was prepared, as shown in Fig. 16(b). The metamaterial wing spar and the wing root were fabricated by SLS and fixed together with screws. The wing ribs, crafted from acrylic plates through laser cutting, were attached to the

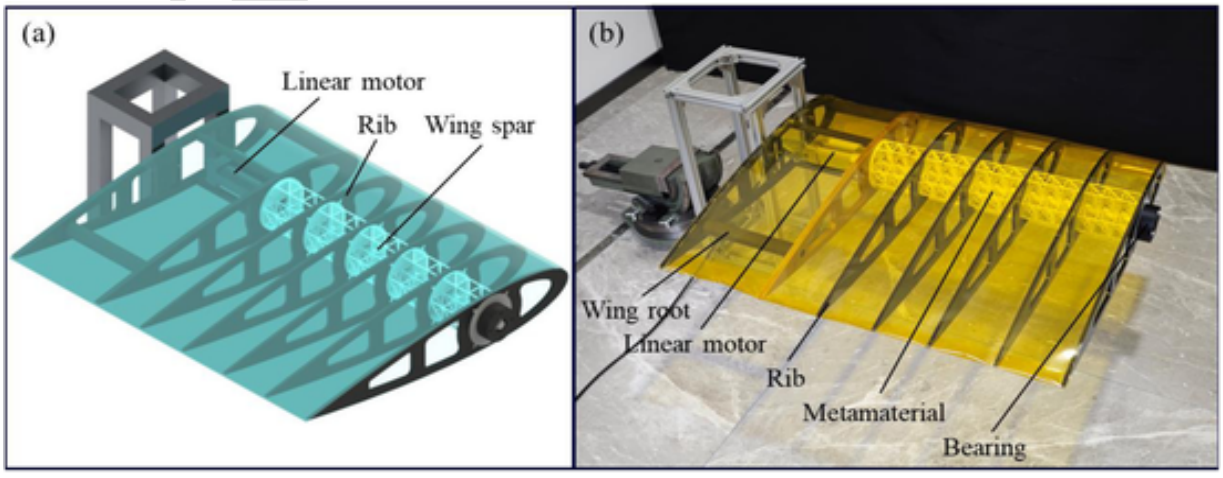

Fig. 16. (a) Design of the twisting wing; (b) The physical prototype of the twisting wing.

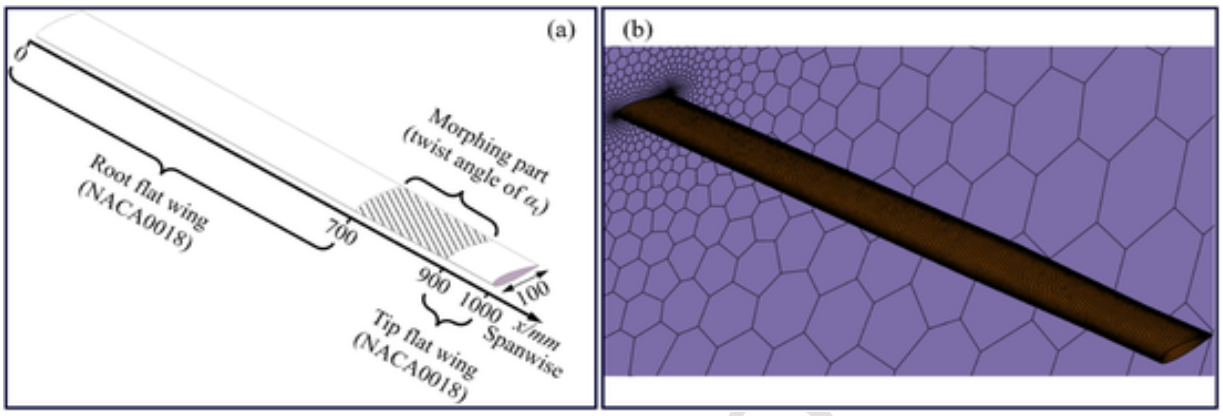

Fig. 17. Designing and fluid model of the morphing wing: (a) Concept for morphing wing using the twisting wing as the morphing part; (b) Meshing of the fluid field and fluid model of the morphing wing.

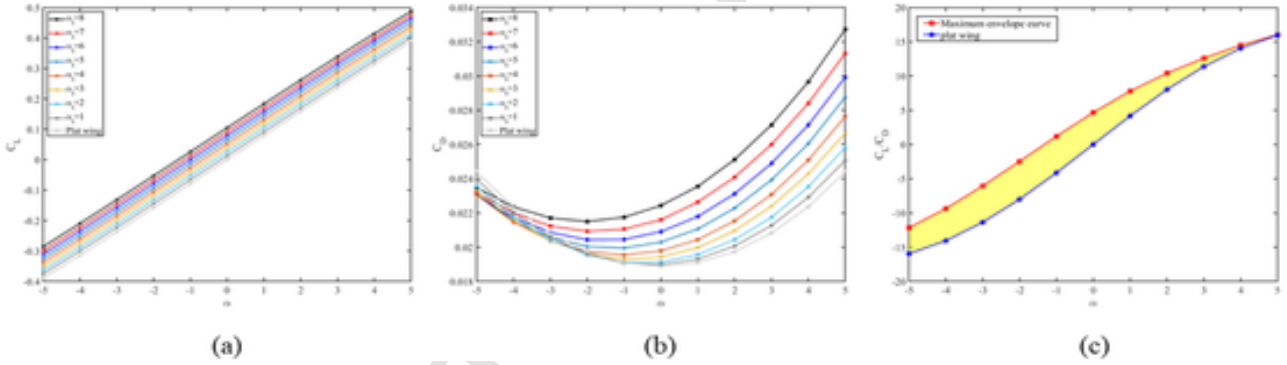

Fig. 18. Aerodynamic characteristics of the morphing wing: (a) Lift coefficient; (b) Drag coefficient; (c) lift-drag ratio.

metamaterial wing spar using mortise and tenon joints. A ball bearing facilitated the connection between the output rod of the linear motor and the other end of the metamaterial spar. The linear motor was placed inside the wing root. The tensile force output from the linear motor causes the wing spar to twist. As measured, it can be found that the twisting wing can produce a twist greater than 8° under a uniaxial tensile force of approximately 1000 N.

4.2. Morphing wing and aerodynamic characteristics

Aerodynamic performance is studied for the proposed morphing wing concept, the twist morphing wing is located near the tip of the wing for improving the aerodynamic characteristics, as shown in Fig. 17(a). A model was created with chord and span lengths of 100 mm and 1000 mm, respectively. The length of the morphing part was designed as 200 mm. The airfoil was selected as NACA0018, and α_t represents the twist angle of the morphing part. The tip flat wing maintains the same angle of attack (α) as the side of the morphing part. When subjected to a changing tension, the morphing part can twist from 0° to 8° ($\alpha_t = 0 \sim 8°$) continuously and smoothly. The influence of the twisting morphing part on the aerodynamic characteristics of the morphing wing was analyzed through the Computational Fluid Dynamics (CFD) simulation using ANSYS FLUENT 2023R2. The numerical simulated state is as follows: the flight speed $v = 30$ m/s, the Reynolds number $Re = 4.0e+7$, the α ranges from −5° to 5° and the α_t ranges from 0° to 8°. The fluid model of the morphing wing was created according to the structural model shown in Fig. 19(a). The fluid field size is 20,000 × 25,000 × 20,000 mm, and the root surface of the morphing wing is defined as a wall. The surface mesh of the morphing wing was refined by regulating the minimum curvature of the surface, as shown in Fig. 17(b). The polyhedral meshing technique was employed for meshing the fluid field with 2.1 million elements.

Fig. 18 shows the lift coefficient, drag coefficient and lift-drag ratio of the morphing wing. It is noted that the lift coefficient of the morphing wings increases linearly with the angle of attack (α) for wings, regardless of the twist angles of the morphing part. Moreover, a linear relation can be found between the lift coefficient of the wing and the twist angle of the morphing part, as the lift coefficient curves exhibit a parallel trend and the difference in values between adjacent curves is almost equal. Likewise, the drag coefficient curves of wings with different twist angles (α_t) of the morphing part exhibit a consistent pattern—an initial decrease followed by a subsequent increase. The twist of the morphing part can improve the drag coefficient of the morphing wing when the α is greater than 0°, and it reverses when α is <0°. The minimum drag coefficient of each curve increases while the corresponding α decreases with the increase of the twist angle. As for the lift-drag ratio of the morphing wing, a notable improvement in the lift-drag ratio beyond the flat wing can be achieved for the morphing wing by adjusting the twist angle, α_t, of the morphing part. As depicted in Fig. 18(c), the yellow region represents the range of improvement in the lift-to-drag ratio of the morphing wing over the flat wing, which reveals the benefits of the twist morphing wing. For $-5° < \alpha \leq 2°$, the morphing wing with $\alpha_t = 8°$ exhibits the maximum lift-drag ratio. At $\alpha = 3°$, the morphing wing with $\alpha_t = 6°$ exhibits the maximum lift-drag ratio. At $\alpha = 4°$, the morphing wing with $\alpha_t = 4°$ exhibits the maximum lift-drag ratio, and at $\alpha = 5°$, the morphing wing with

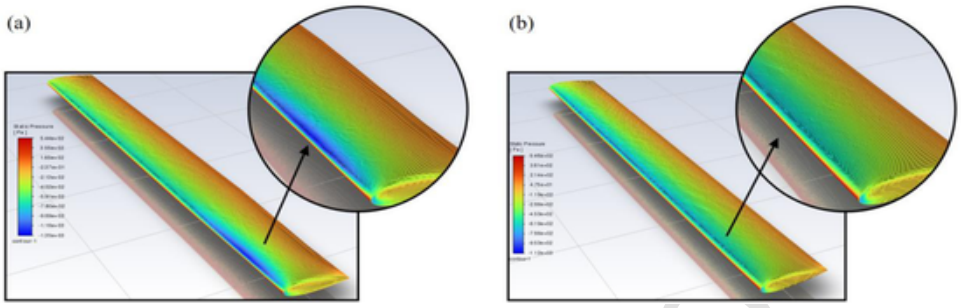

Fig. 19. Static pressure of the morphing wing: (a) $\alpha = 5^{\circ}$ and $\alpha_t = 7^{\circ}$; (b) $\alpha = 5^{\circ}$ and $\alpha_t = 0^{\circ}$.

$\alpha_t = 3^{\circ}$ exhibits the maximum lift-drag ratio. Adjusting the twist angle of the morphing part adaptively according to the α of the root flat wing enables the morphing wing to optimize the lift-to-drag ratio when α is changing. The maximum increase in lift-drag ratio is 5.5390, which occurs at $\alpha = -2^{\circ}$ between the morphing wing with an morphing part twist of 8° and the flat wing.

Fig. 19 depicts the distribution of static pressure on the surface of the morphing wing with an angle of attack (α) of 5° and a twist angle (α_t) of 7°. Compared to the flat wing ($\alpha_t = 0^{\circ}$) at $\alpha = 5^{\circ}$, introducing the twist of the morphing part significantly influences the static pressure distribution on the surface of the morphing wing. A moving of the negative airfoil pressure on the upper surface towards the tip of the morphing part. Additionally, the negative pressure decreases than the flat wing which leads to an increase in the lift coefficient.

5. Conclusion

A novel tension-twist coupling morphing wing has been proposed. It uses a designed twisting wing as the morphing part, which can produce a considerable, continuous and adjustable spanwise twist deformation during axial stretching. To achieve this, a tension-twist coupling metamaterial cantilever is applied to the spar of a morphing wing. The tension-twist coupling deformation is achieved by assembling the tension-shear coupling deformation of the unit cells through cell stacking. The sizes of the unit cells and the stacking strategies are critical for achieving the targeted coupling effect and assembly of the twist deformation. The morphing wing using the tension-twist coupling metamaterials demonstrates a significate improvement in aerodynamic characteristics, lift coefficient and lift-drag ratio. This morphing wing combines the variable-span wing and the twisting wing, allowing for adaptive twist angle adjustments of the morphing part to optimize aerodynamic performance. The introduction of tension-twist coupling metamaterials enables the realization of multi-dimensional deformation and simplification of the drive mechanism.

CRediT authorship contribution statement

Zhu Xueren: Writing – original draft, Validation, Investigation, Formal analysis. **Zhang Jiaying:** Writing – review & editing, Supervision. **Chen Wei:** Supervision, Data curation. **Huaiyuan Gu:** Writing – review & editing, Methodology.

Declaration of competing interest

The authors declare that they have no known competing financial interests or personal relationships that could have appeared to influence the work reported in this paper.

Acknowledgments

This project has received funding from National Natural Science Foundation of China (Grant No 92271104, 12102017) and Beijing Natural Science Foundation (Grant No 1232014).

Data availability

No data was used for the research described in the article.

References

[1] S. Barbarino, O. Bilgen, R.M. Ajaj, et al., A review of morphing aircraft, J. Intell. Mater Syst. Struct. 22 (9) (2011) 823–877.
[2] R. Decamp, R. Hardy, Mission adaptive wing advanced research concepts, in: 11th Atmospheric Flight Mechanics Conference, 1984, p. 2088.
[3] A.K. Jha, J.N Kudva, Morphing aircraft concepts, classifications, and challenges, in: Smart structures and materials 2004: industrial and commercial applications of smart structures technologies. SPIE, 5388, 2004, pp. 213–224.
[4] B. Liu, H. Liang, Z.H. Han, et al., Surrogate-based aerodynamic shape optimization of a morphing wing considering a wide Mach-number range, Aerosp. Sci. Technol. 124 (2022) 107557.
[5] S.B. Smith, D.W. Nelson, Determination of the aerodynamic characteristics of the mission adaptive wing, J. Aircr. 27 (11) (1990) 950–958.
[6] X. Hang, W. Su, Q. Fei, et al., Analytical sensitivity analysis of flexible aircraft with the unsteady vortex-lattice aerodynamic theory, Aerosp. Sci. Technol. 99 (2020) 105612.
[7] J.J. Spillman, The use of variable camber to reduce drag, weight and costs of transport aircraft, Aeronautic. J. 96 (951) (1992) 1–9.
[8] J. Zhang, A.D. Shaw, C. Wang, et al., Aeroelastic model and analysis of an active camber morphing wing, Aerosp. Sci. Technol. 111 (2021) 106534.
[9] L. Wang, Z. Xu, T. Yue, Dynamic characteristics analysis and flight control design for oblique wing aircraft, Chinese J. Aeronautic. 29 (6) (2016) 1664–1672.
[10] S. Yi, L. Shen, C.Y. Wen, et al., Aerodynamic performance of a nanostructure-Induced multistable Shell, Aerospace 8 (11) (2021) 350.
[11] Boeing. Variable camber wing[EB/OL]. [2024-01-03] https:‖apps.dtic.mil/sti/citations/AD0911543.
[12] M. Love, S. Zink, R. Stroud, et al., Impact of actuation concepts on morphing aircraft structures, in: 45th AIAA/ASME/ASCE/AHS/ASC Structures, Structural Dynamics & Materials Conference, 2004, p. 1724.
[13] E. KAYGAN, C. Ulusoy, Effectiveness of twist morphing wing on aerodynamic performance and control of an aircraft, J. Aviat. 2 (2) (2018) 77–86.
[14] J. Zhang, C. Bisagni, Buckling-driven mechanisms for twisting control in adaptive composite wings, Aerosp. Sci. Technol. 118 (2021) 107006.
[15] M. Majji, O. Rediniotis, J. Junkins, Design of a morphing wing: modeling and experiments, in: AIAA Atmospheric Flight Mechanics Conference and Exhibit, 2007, p. 6310.
[16] B. Luo, W. Cui, W Li, Active and robust twisting morphing wings with geometric constraints for flying or swimming robots, IEEE/ASME Transa. Mechatronic. 27 (5) (2022) 4205–4210.
[17] H. Yang, S. Jiang, Y. Wang, et al., Fluid–structure coupling and aerodynamic performance of a multi-dimensional morphing wing with flexible metastructure skin, Aerospace 10 (8) (2023) 678.
[18] J. Sun, Q. Guan, Y. Liu, et al., Morphing aircraft based on smart materials and structures: a state-of-the-art review, J. Intell. Mater. Syst. Struct. 27 (17) (2016) 2289–2312.
[19] R.N. Saunders, D.J. Hartl, J.G. Boyd, et al., Modeling and development of a twisting wing using inductively heated shape memory alloy actuators[C]//Active and passive smart structures and integrated systems 2015, SPIE 9431 (2015) 263–270.
[20] N. Kim Pham, E.A Peraza Hernandez, Design exploration of a tensegrity-based twisting wing, in: International Design Engineering Technical Conferences and

Computers and Information in Engineering Conference. American Society of Mechanical Engineers, 83990, 2020 V010T10A072.
[21] J. Sun, X. Li, Y. Xu, et al., Morphing wing based on trigonal bipyramidal tensegrity structure and parallel mechanism, Machines 10 (10) (2022) 930.
[22] Y. Chen, M.H Fu, A novel three-dimensional auxetic lattice meta-material with enhanced stiffness, Smart Mater. Struct. 26 (10) (2017) 105029.
[23] P. Xu, X. Lan, C. Zeng, et al., Compression behavior of 4D printed metamaterials with various Poisson's ratios, Int. J. Mech. Sci. 264 (2024) 108819.
[24] X. Zheng, H. Lee, T.H. Weisgraber, et al., Ultralight, ultrastiff mechanical metamaterials, Science (1979) 344 (6190) (2014) 1373–1377.
[25] T. Tancogne-Dejean, M. Diamantopoulou, M.B. Gorji, et al., 3D plate-lattices: an emerging class of low-density metamaterial exhibiting optimal isotropic stiffness, Adv. Mater. 30 (45) (2018) 1803334.
[26] D. Qi, P. Zhang, W. Wu, et al., Innovative 3D chiral metamaterials under large deformation: theoretical and experimental analysis, Int. J. Solids Struct. 202 (2020) 787–797.
[27] N. Hao, L. Zhu, Z. Wu, et al., A Novel 3D-printed Unit Cell With the Compression-Torsion Coupling Effect and Negative Poisson's ratio[C]//Structures, 63, Elsevier, 2024 106467.
[28] B. Jenett, S. Calisch, D. Cellucci, et al., Digital morphing wing: active wing shaping concept using composite lattice-based cellular structures, Soft. Robot. 4 (1) (2017) 33–48.
[29] Cramer N., Croom M., Cheung K., et al. Design and testing of a cellular composite active twist wing. 2016 AIAA SciTech Conference. 2016 (NF1676L-23323).
[30] T. Johnson, M. Frecker, M. Abdalla, et al., Nonlinear analysis and optimization of diamond cell morphing wings, J. Intell. Mater. Syst. Struct. 20 (7) (2009) 815–824.
[31] A. Büter, U.C. Ehlert, D. Sachau, et al., Adaptive rotor blade concepts: direct twist and camber variation, in: AVT Symposium, Braunschweig, 2000.
[32] X. Chen, T. He, Y. Hu, et al., A 3D dislocated re-entrant structure with compression-twist coupling effect, Smart Mater. Struct. 32 (5) (2023) 055009.
[33] D. Goswami, Y. Zhang, S. Liu, et al., Mechanical metamaterials with programmable compression-twist coupling, Smart Mater. Struct. 30 (1) (2020) 015005.
[34] K. Yang, L. Rao, L. Hu, et al., 3D curved-walled same-phase chiral honeycombs with controllable compression-torsion coupling effect via variable cross-section design, Thin-Walled Struct. 193 (2023) 111267.
[35] J. Zhou, J. Chang, X. Song, et al., Bio-inspired design and unusual mechanical properties of 3D horseshoe-shaped soft network metamaterials, Composites Part B: Eng. (2024) 111284.
[36] Y. Wang, C. Lai, H. Cao, et al., Metastructure with torsion-compression coupling behaviors: additive-manufacturing, experimental and numerical investigations, Compos. Struct. 322 (2023) 117418.
[37] K. Yang, L. Rao, L. Hu, et al., 3D curved-walled same-phase chiral honeycombs with controllable compression-torsion coupling effect via variable cross-section design, Thin-Walled Struct. 193 (2023) 111267.
[38] T. Frenzel, M. Kadic, M. Wegener, Three-dimensional mechanical metamaterials with a twist, Science (1979) 358 (6366) (2017) 1072–1074.
[39] R. Zhong, M. Fu, X. Chen, et al., A novel three-dimensional mechanical metamaterial with compression-torsion properties, Compos. Struct. 226 (2019) 111232.
[40] B.B. Zheng, R.C. Zhong, X. Chen, et al., A novel metamaterial with tension-torsion coupling effect, Mater. Des. 171 (2019) 107700.
[41] L.R. Long, M.H. Fu, L.L Hu, Novel metamaterials with thermal-torsion and tensile-torsion coupling effects, Compos. Struct. 259 (2021) 113429.
[42] H. Gu, A.D. Shaw, M. Amoozgar, et al., Twist morphing of a composite rotor blade using a novel metamaterial, Compos. Struct. 254 (2020) 112855.
[43] H. Gu, J. Taghipour, A.D. Shaw, et al., Tailored twist morphing achieved using graded bend–twist metamaterials, Compos. Struct. 300 (2022) 116151.
[44] H. Yang, S. Jiang, Y. Wang, et al., Design, kinematic and fluid-structure interaction analysis of a morphing wing, Aerosp. Sci. Technol. 143 (2023) 108721.
[45] C. Peng, P. Tran, H. Nguyen-Xuan, et al., Mechanical performance and fatigue life prediction of lattice structures: parametric computational approach, Compos. Struct. 235 (2020) 111821.